Analytical Modeling of Misalignment in Axial Flux Permanent Magnet Machine

Guo, Baocheng; Huang, Yunkai; Peng, Fei; Dong, Jianning; Li, Yongjian

DOI
10.1109/TIE.2019.2924607

Publication date
2020

Document Version
Final published version

Published in
IEEE Transactions on Industrial Electronics

Analytical Modeling of Misalignment in Axial Flux Permanent Magnet Machine

Baocheng Guo, *Member, IEEE*, Yunkai Huang, Fei Peng, *Member, IEEE*, Jianning Dong, *Member, IEEE*, and Yongjian Li, *Member, IEEE*

***Abstract*—This paper proposes an analytical model for the prediction of air gap magnetic field distribution for axial flux permanent magnet (AFPM) machine with various types of misalignments. The AFPM machine geometry is first transformed to a polar representation. Consequently, the subdomain model based on current sheet technique is developed. Then the stator coordinate system is chosen as reference coordinate to consider both static/dynamic angular and axis misalignments. The back electromagnetic forces and cogging torque are obtained accordingly based on Maxwell's equations. The results show that the proposed approach agrees with the finite-element method. The model is further validated by experiments under healthy, dynamic angular and axis misalignment conditions, which can validate the proposed approach. It turns out that the proposed approach can predict the performance of AFPM machines with types of misalignment quickly and effectively, which is greatly significant for further fault detection.**

***Index Terms*—Axial flux permanent magnet (AFPM) machine, current sheet model, magnetic field, misalignment.**

I. Introduction

AXIAL flux permanent magnet (AFPM) machines, due to their compact mechanical structure and high power density, are promising in many industrial applications, such as the electric vehicles [1], [2], wind power generation [3], and flywheel energy storage system. However, the rotor misalignment is still remaining as one of the major problems of AFPM machines. Rotor misalignment for AFPM is not only caused by the common reasons as we know, viz., bearing faults and manufacturing imperfections, but is also affected by its own mechanical feature. More specially, the contact area between the shaft and inner rotor is relative small and axial force between stator and rotor is high. Mark [4] indicated that the misalignment of AFPM machines can be categorized as angular and axis misalignment as shown in Fig. 1, which is different from and more complex than that of radial flux permanent magnet (RFPM) machines. Rotor misalignment can result in disordered magnetic field distribution (MFD), and hence cause serious problems, for instance, unbalanced magnetic force and mechanical vibration [5], which will affect normal operation and safety. Therefore, the defects should be analyzed and detected quickly to avoid further damages.

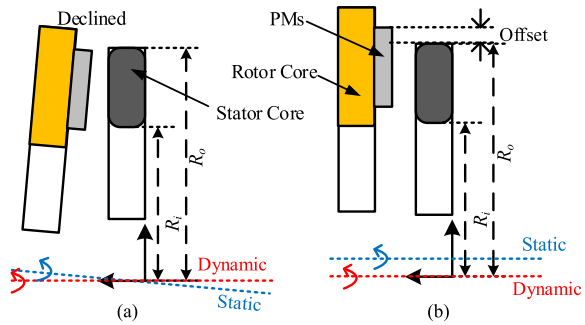

Fig. 1. Configuration of misalignment for AFPM machine. (a) Angular misalignment. (b) Axis misalignment.

A significant amount of work has been done concerning the misalignment of AFPM machines. At present, the finite-element (FE) method (FEM) is widely used in misalignment simulation since it is regarded as the most accurate method. Gerlando [6] adopted FE approach and field functions to investigate the misalignment. However, under such conditions, the nonuniform air-gap region of AFPM machine requires a three-dimensional (3-D) FE model and a high-quality meshing, which results in long computation time. An alternative method to reduce the computation time is the field reconstruction (FR) method, which is partly based on the FEM model. Ajily [7] adopted the FR approach to study the rotor eccentricity. Although it is much faster than 3-D FE models, it still requires considerable computation time.

Analytical or semianalytical approaches, due to their fast and acceptable accuracy, are regarded as efficient and favorable methods. The magnetic equivalent circuit (MEC) method, although the MEC method can improve computation efficiency,

Manuscript received August 1, 2018; revised October 25, 2018, December 26, 2018, and May 27, 2019; accepted June 5, 2019. Date of publication June 28, 2019; date of current version February 10, 2020. This work was supported in part by the National Nature Science Foundation of China under Project 51777034, in part by the State Key Laboratory of Reliability and Intelligence of Electrical Equipment, Hebei University of Technology, under Project EERIKF2018009, and in part by the Qing Lan Project. *(Corresponding author: Baocheng Guo.)*

B. Guo, Y. Huang, and F. Peng are with the School of Electrical Engineering, Southeast University, Nanjing 210096, China (e-mail: guobaocheng1986@gmail.com; huangyk@seu.edu.cn; pengfei@seu.edu.cn).

J. Dong is with the Department of Electrical Sustainable Energy, Delft University of Technology, 2628CD Delft, The Netherlands (e-mail: J.Dong-4@tudelft.nl).

Y. Li is with the State Key Laboratory of Reliability and Intelligence of Electrical Equipment, Hebei University of Technology, Tianjin 300130, China (e-mail: liyongjian@hebut.edu.cn).

Color versions of one or more of the figures in this paper are available online at http://ieeexplore.ieee.org.

Digital Object Identifier 10.1109/TIE.2019.2924607

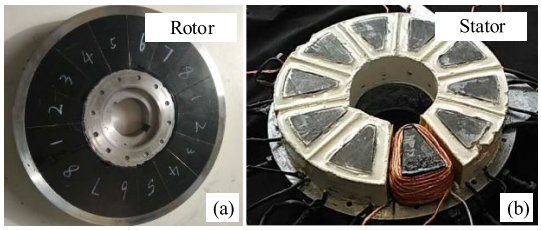

Fig. 2. Configuration of the AFPM machine. (a) Rotor. (b) Stator.

it is complicated to build up the MEC model for the whole machine. Alternative analytical solutions are appearing in the literature [8], which is based on the solution of Poisson's and Laplace's equations. Some researchers have used either the perturbation method combining with the subdomain method to analytically model the rotor eccentricity for RFPM machines. However, the methods are too complex. As studied in [9], the length function of permanent magnets (PMs) is introduced to consider the manufacturing imperfections; however, for machines with Halbach arrays, this approach is too complicated. From literature survey, most literatures concern on the rotor eccentricity of RFPM machines, and previous studies do not provide a simple, general, and accurate subdomain solution for both angular and axis misalignments of AFPM machines.

To overcome aforementioned problems, an analytical model (AM) based on subdomain technique is proposed to predict the MFD and performance of AFPM machines with angular and axis misalignment. In this paper, the geometry of AFPM machine is first transformed to the polar coordinate system. Then the model can be developed based on the same theory as that for RFPM machines. Compared to existing literatures, the proposed method is more straightforward and easy to implement. Moreover, the characteristics of AFPM machine with various misalignments are explored and explained. On the other hand, the AM cannot consider the in-plane flux densities, which is inherent limitation of most AMs. Comparing with FE method, the AM has lower CPU time and acceptable accuracy, and hence, it can be regarded as an effective tool to study the misalignments.

This paper is organized as follows. In Section II, the parameters of the prototype are provided. Section III introduces the equivalent principle of AFPM to RFPM, and the subdomain model for normal, angular, and axis misalignment based on current sheet technique are also expressed in this section. Afterward, the results are then discussed in Section IV. In section V, the experiment results are presented and compared with the results obtained from the proposed approach. Section V concludes this paper.

II. Model of Misalignment in AFPM

In this paper, a 10-slot/4-pole 5-phase AFPM machine with concentrated coils is introduced to validate the proposed method, as shown in Fig. 2. The PM with low remanence (bonded type) and amorphous magnetic material (AMM) with high relative permeability are adopted to reduce the iron loss under high operating frequency. These features match well with the linearity assumptions made in the analytical approach, it turns out that acceptable results could be obtained by using AM. However, this machine has to be designed with an open slot topology because of the cutting technique and material properties of AMM [10]. Thanks to the Halbach array, flux density in the air gap can be improved to the acceptable level even with open slots.

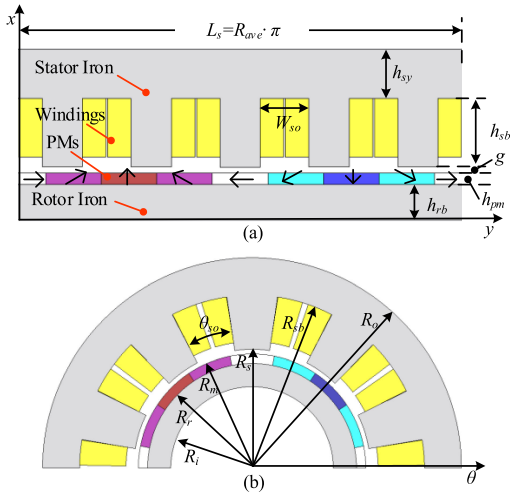

Fig. 3. Analytical model for AFPM machine. (a) Analytical model in Cartesian coordinates. (b) Converted model in polar coordinates.

A quasi-3-D method is used to convert a 3-D model to a two-dimensional (2-D) model to reduce the computation time. The machine is divided into a number of layers with a cylindrical cross section. Afterward, the AFPM can be considered to be composed of several 2-D calculation planes as shown in Fig. 3(a). In order to simulate partial magnet demagnetization at different location and obtain more accurate results, five slices are chosen in this paper. The average radius $R_{\rm ave}$ of the kth layer is given by

$$R^k_{\rm ave} = R^a_i + \frac{R^a_o - R^a_i}{2n_s}(2k-1), \quad k = 1, 2, ..., n \tag{1}$$

$$t_{cp} = \frac{R^a_o - R^a_i}{n_s} \tag{2}$$

where n_s is the number of the slices, and t_{cp} is the width of the slices.

A. Conversion of Calculation Coordinates

Fig. 3(a) shows one layer of the 2-D AM of AFPM in the Cartesian coordinate system. The parameters of the AFPM are as follows: L_s is the length of computational domain, h_{rb} is the height of the back-iron, h_{pm} is the height of the PMs, h_{sb} is the depth of slots, h_{sy} stands for the height of stator back iron, and w_{so} stands for the slot opening width. In order to propose a general analytical solution, the equivalent analytical technique to approximate the AFPM as a RFPM presented in [11] is adopted. Fig. 3(b) shows the equivalent RFPM.

It should be noted that this is an approximated approach; therefore, the transformation obtained by different reference component may result in slight errors in results. In this paper, the equivalent mean air-gap radius $R_{\rm ave}$ of k_{th} layer is kept unchanged in the equivalent. The relationship between the dimensions of the equivalent RFPM and the AFPM are listed in

TABLE I
RELATIONSHIPS BETWEEN TWO COORDINATES

Symbol	RFPM QUANTITY	Equivalent Value
R_s	Stator inner radius	$R_{ave} + g_0/2$
R_{sb}	Stator yoke radius	$R_s + h_{sb}$
R_o	Stator outer radius	$R_{sb} + h_{sy}$
R_m	Radius of PMs	R_{ave} - $g/2$
R_r	Rotor outer radius	R_m - h_{pm}
R_i	Rotor inner radius	R_r - h_{rb}
θ_{so}	Slot opening	W_{so}/R_{ave}
L	Equivalent core length	t_{cp}

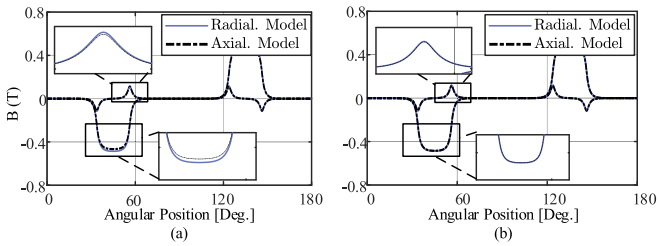

Fig. 4. Influence of correction factor. (a) Before correction. (b) After correction.

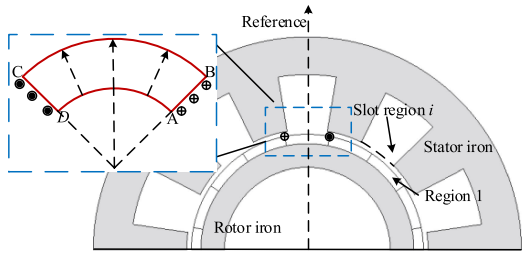

Fig. 5. Subdomain model.

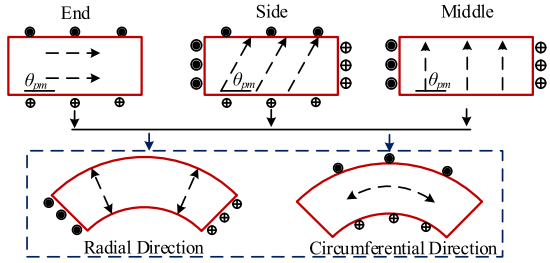

Fig. 6. PM under different magnetization.

Table I. It should be noted that the average radius $R_{\rm ave}$ of each slice should be converted according to this principle.

Therefore, the AM of AFPM in Cartesian coordinate system is converted to a polar system, as shown in the above-mentioned equivalent approximation. However, comparing with [11], no extended air region is added in to ensure the results; a slight error in the amplitude will occur. Therefore, the equivalent AM in this paper needs a correction factor (f_B) to calibrate the final results as

$$B_r(\theta) = f_B \cdot B_{rp}(\theta), B_t(\theta) = f_B \cdot B_{tp}(\theta) \tag{3}$$

where B_{rp} and B_{tp} are the radial and tangential components obtained in polar coordinate, respectively. B_r and B_t are the final axial and radial components in Cartesian system.

The slotless AM developed in Cartesian [12] and polar [13] coordinates are adopted to investigate the influence of coordinate transformation. Fig. 4(a) shows the radial air gap flux density component of single PMs with 90° magnetization direction (MD) without correction. As expected, it can be seen in that the error comes. In [14], the ratio between the magnet radial thickness h_{pm} and the mean air-gap radius R_{av} of each layer is selected as the parameter. It can be seen that the correction factor is determined on the condition that the ratio is given.

More detailed information and the curvature can be found in [14], hence, not repeated here. Although the difference is little for AFPM machine in this paper, the correction factor is still need to be applied to the final flux density results in order to achieve higher accuracy, as shown in Fig. 4(b).

B. Equivalent Surface Current of Magnet

The subdomain is chosen to calculate the magnetic field. Normally, several assumptions are made to simplify the calculation:

1) the iron materials have infinite permeable;
2) the end effect and eddy current effect are ignored;
3) the magnetic material has uniform magnetization, and the relative recoil permeability μ_r is constant.

It should be noted that the end effect is ignored in this paper. One of the reasons is that the flux drop at the end slices is relative small (6%) under normal condition. Moreover, the Halbach arrays and the various types of misalignments will increase the complexity of the end effect significantly. A detailed discussion of the end effect goes beyond the scope of this paper; it will be published separately. In spite of the end effect being ignored, the analytical solutions are sufficiently accurate to predict EM performance, which can be seen in later section.

The current sheet technique based on [15] is selected in this paper. The calculation model can be seen in Fig. 5. Afterward, the exact SD model can be separated into two domains, viz., air gap and PM region (region 1) and slot region (region 2*i*). The magnetization of PM in AFPM is in parallel since the PMs are flat, however, after converting it into the polar system, it is noticed that the magnetization is also changed. The MD is changed to radial.

For radial magnetization, the linear current density of sides AB and CD can be presented as

$$J = H_{cj} \tag{4}$$

where H_{cj} is the coercivity of PM.

It should be noted that the AFPM machine investigated in this paper has Halbach arrays, 4-segment array is chosen in this machine and the PMs can be defined as end, side, and middle PM, as shown in Fig. 6. Different magnetization can be replaced by combining radial and circumferential magnetization.

Subsequently, the PMs are divided into a number of current sheets at radius with a linear current. The total current of the

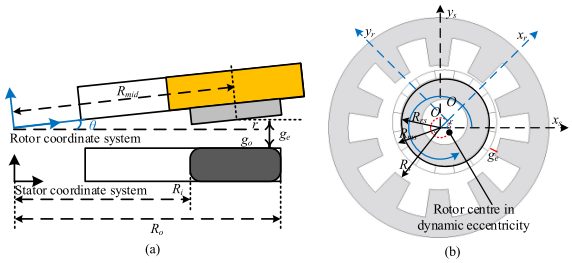

Fig. 7. (a) Configuration of angular misalignment. (b) Angular misalignment illustration under polar coordinate.

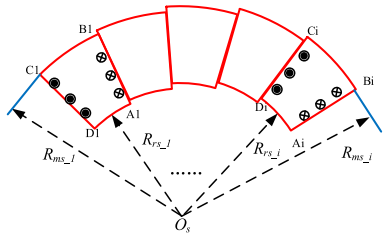

Fig. 8. Configuration of sections of PM.

equivalent coil can be expressed as

$$i_c = J_x \Delta l \tag{5}$$

where J_x is the radial and circumferential current density shown in (5). Δl is the length infinitesimal in the sides AB, CD, AD, and BC of the magnet pole.

Hence, the magnetization vector $\boldsymbol{M}$ can be replaced by a pair of magnetizing currents i_c, and the radial and tangential flux density components of single PM. In [14], the detailed mathematic model and general expressions of each domain for normal condition of this prototype can be found. Combining with the continue boundary conditions, the unknown coefficients are solved in MATLAB environment and the total MFD is then obtained by superposition of each PM and, hence, not repeated here. In this paper, the various misalignments are investigated.

C. Model of Angular Misalignment

The angular misalignment is caused by the slant rotor plate. The static/dynamic angular misalignment could be presented by Fig. 7(a).

In order to model the angular misalignment, it is necessary to evaluate the air-gap length at any radius. The static eccentricity factor (f_{se}) could be defined as [16]

$$f_{se} = r/g_0 \tag{6}$$

where r is the length which deviate from the normal air-gap length g_0. And finally, the air-gap length of static angular misalignment for static reference frame can be deduced as

$$g_e = g_0 \left(1 - \frac{R}{R_{\text{mid}}} f_{se} \cos(\varphi - \gamma_0 - k_d \omega t)\right) \tag{7}$$

where R_{mid} is mean radius and φ is the position measured from a reference point (γ_0) of the minimal air gap, ω is rotation speed in rad/s, and t is the time. k_{ang} is the coefficient, which determines the type of angular misalignment. When k_{ang} is 0, it is static misalignment, if it equals 1, it is dynamic misalignment.

And hence, it can be converted to the polar coordinate; the angular misalignment can be shown in Fig. 7(b). With regard to the angular misalignment, the approximate method presented in [17] is adopted in this paper to predict the performance of AFPM machines. On the one hand, as mentioned above, it is complex when adopting the perturbation method because more unknown coefficients should be introduced. On the other hand, considering the axis misalignment calculated later, it would be better to develop based on the similar calculation theory and work out to be a calculation system, which is easy to understand and accomplish.

It should be noticed that the reference center in this paper is selected at the stator geometry center, as shown in Fig. 7(b), which is different with [17]. After that, the parameters related to the stator system, such as the positions of the stator slot opening parameters, slot tooth parameters, slot body parameters, and stator yoke thickness, will not be changed when there is an angular misalignment, which is good for armature effect calculation. By doing this, only parameters for one subdomain (PM and air gap) is changed, which reduces the calculation complexity of misalignment problem.

These different air-gap lengths can be calculated according to (7), and hence, the radius of outer rotor (R_{rs}) and the radius of PMs (R_{ms}) under angular misalignment can be determined. For example

$$R_{ms} = R_s - g_e. \tag{8}$$

Afterward, the PM of eccentric machine can be divided into several uniform sections along the air-gap circumferential direction, as shown in Fig. 8. The points that determine the equivalent air-gap length of each section are chosen at the intersections of each section center line. It should be noted that the section of PMs can be expressed by a pair of current sheet, which means the MFD of each section can be calculated individually. Therefore, the current sheet approach presented in this paper is more suitable for predicting the MFD of misaligned PM by using superposition principle.

In theory, the section number (N_s) of PM can be any positive integer, and the results obtained by the proposed method will be more accurate if it is larger. However, it will lose the merit of highly efficient computation when the section number is too large, while it cannot also be too small to guarantee the accuracy of results. Based on principle presented in [17], each slot opening center should belong to a section, and the section number is better chosen as three times of the stator slot number for most of electrical machines. However, the reference center is stator in this paper and the PMs of investigate machine are spread all over at rotor outer diameter. Therefore, it needs to reinvestigate the influence of section number on MFD to ensure the accuracy. This will be investigated later.

D. Model of Axis Eccentricity

The axis misalignment occurs when the stator and rotor are offset from each other in the axis direction, as shown in Fig. 10.

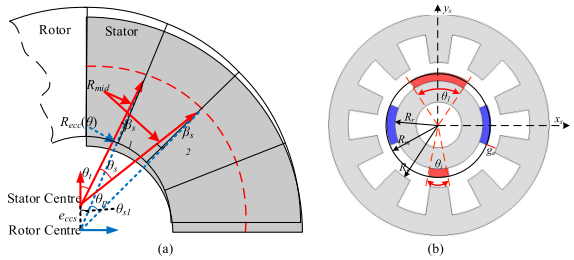

Fig. 9. (a) Configuration of axis misalignment. (b) Axis misalignment illustration under polar coordinate.

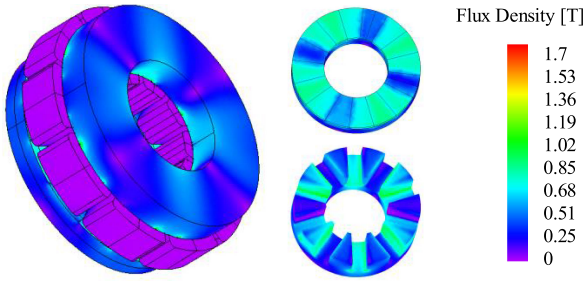

Fig. 10. FE model.

In order to reduce the complexity of the axis misalignment computations, the parts of poles overhanging the outer radius and the inner radius of the stator are ignored.

As for the axis misalignment, the reference center of computational coordinate is also selected at the stator geometry center, as shown in Fig. 9(a). After that, the parameters related to the stator system are still unchanged when there is an axis misalignment. However, the PM length needs some minor changes, since the reference frame is fixed on the stator, which is caused by the overhanging effect.

Take the mean radius as an example, the actual PM angle θ_s under axis misalignment can be deduced as

$$R_{ecc} = \sqrt{{R_{\rm mid}}^2 + e_{ccs}^2 - 2R_{\rm mid}e_{ccs}\cos(\pi - \theta_t + k_d\omega t)} \tag{9}$$

$$\beta_{s1} = \arccos\left(\frac{R_{\rm mid}^2 + R_{ecc}^2 - e_{ccs}^2}{2R_{\rm mid}R_{ecc}}\right) \tag{10}$$

$$\beta_{s2} = \arcsin\left(\frac{e_{ecc}\sin(\theta_{s1} + \theta_p)}{R_{\rm mid}}\right) \tag{11}$$

where e_{ccs} is the maximum offset distance and $\theta_t. = \theta_t - \theta_{s1}$ is the angle shown in Fig. 8(a). θ_t is the starting angle of the PM in stator coordinate, and θ_p is the opening angle of the PM in rotor coordinate. Hence, based on law of sine and cosine, the actual PM angle θ_s can be determined by β_{s1}, β_{s2} and other θ_p.

It should be noted that the $k_{\rm axis}$ also determines the type of axis misalignment. However, based on the definition in [18], when $k_{\rm axis}$ is 0, it is dynamic axis misalignment, and if it equals 1, it is static axis misalignment. This is much different from the angular misalignment defined above. After obtaining the actual PM opening angle, it can be converted to the polar coordinate and shown in Fig. 9(b). And hence, the single PM can be calculated by aforementioned current sheet approach.

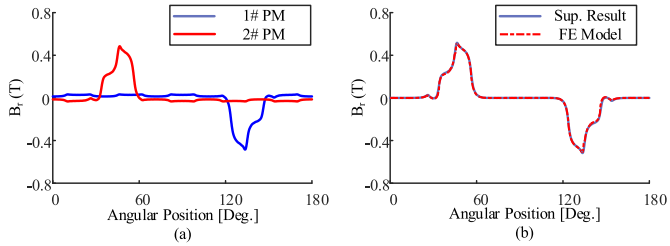

Fig. 11. No-load air-gap flux density waveforms. (a) Single PMs. (b) After superposition.

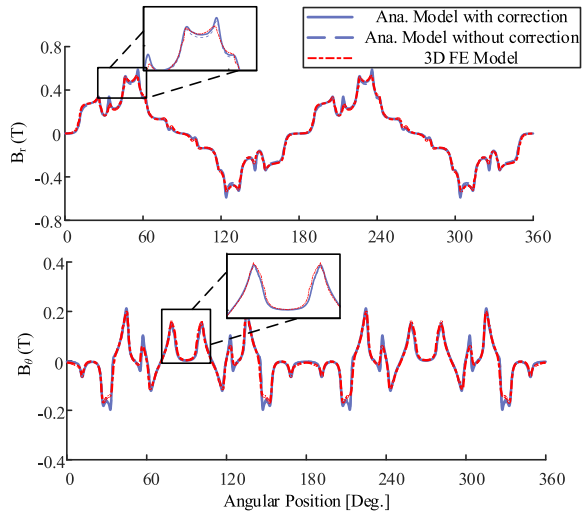

Fig. 12. No-load air-gap flux density waveforms of proposed method and FEM under normal condition.

III. Results and Analysis

A. Normal Performance

The proposed method is verified by 3-D nonlinear time-stepping FEM model as shown in Fig. 10. The JMAG commercial software package is used to carry out the simulation. As for the 3-D FE model, the nonlinear magnetic material AMM is introduced in order to get reliable results. Moreover, the MD function provided by JMAG software is used to model the PM with different MD. Afterward, the MD vector is defined for each PM accordingly. The MD of middle, side, and end PM are 90°, 35°, and 0°, respectively.

Fig. 11(a) shows the radial air-gap flux density component of single PMs with 90° MD. It can be seen that the single PM can be modeled by using the proposed approach, and this feature is more straightforward and convenient to model the variance of each PM. After superposition applied, the magnetic flux distribution is shown in Fig. 11(b). It can be seen that the results match well with FE results.

Fig. 12 compares the flux density in the middle circle of the air gap. Evidently, AM models have disadvantages; one of drawbacks is that they sometimes have to assume infinite permeability of soft magnetic materials. This is, however, not a big issue for high speed PM machines. Due to their high speed operation and large effective air gap, these machines are

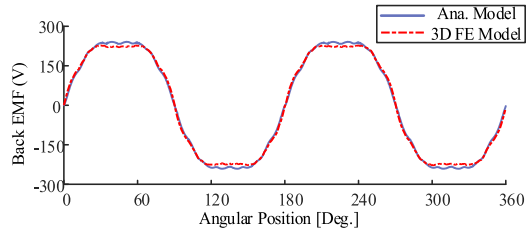

Fig. 13. Back EMF under normal condition.

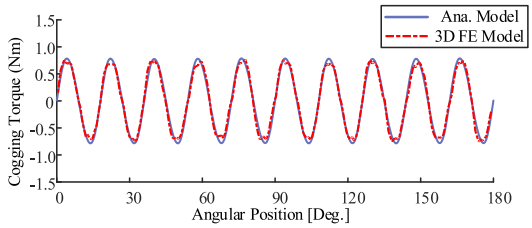

Fig. 14. Comparison of cogging torque.

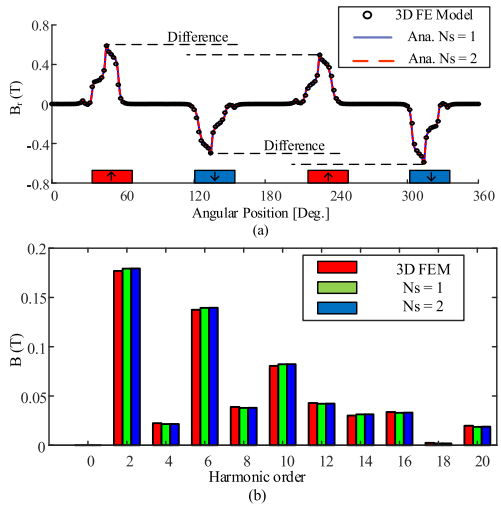

Fig. 15. Air-gap flux density waveforms of demagnetization PMs and FEM. (a) Radial component. (b) Tangential component.

typically operated in the linear region of their magnetic materials. Moreover, the AMM material has a relative large permeability. Therefore, Fig. 12 shows that the results predicted by the proposed method agree well with those obtained from the FEM model. Moreover, it can be seen that the correction factor is still effective when the slot effect is considered.

The back electromotive force (EMF) can be derived as

$$E_j = d\varphi_j/dt \tag{12}$$

where the flux over each slot (φ_j) is

$$\varphi_j = N_c \cdot \int_{\theta_0}^{\theta_0+\theta_c} F_{Dc,s} B_r(R_a,\theta) d\theta \tag{13}$$

where N_c is the number of turns in series per phase, θ_0 is the coil starting side angle from the origin, θ_c is the expansion angle of the coil pitch, F_{Dc} is coil distribution function can be found in [19].

According to the Maxwell tensor equation, the torque can be computed by

$$T = \frac{LR_a^2}{\mu_0} \int_0^{2\pi} B_r(R_a,\theta) \cdot B_t(R_a,\theta) d\theta \tag{14}$$

where L is axial length, R_a is the average radius of air gap.

Hence, the magnetic performance of AFPM machine could be obtained by superimposing the contribution of each layer.

The back EMF is shown in Fig. 13. The computation is done at rated speed 15 000 r/min. The results obtained from the proposed method are in agreement with the FEM ones. The rms value of proposed method is 191.93 and 185.55 for 3-D FEM; it is slightly higher than that of 3-D FEM model. This is mainly caused by the end effect, which means the amplitude of magnetic flux density is dropped at the inner and outer radii. Again, thanks to the Halbach arrays technique, acceptable back EMF could be obtained by designing the MD of PMs.

Fig. 14 shows the cogging torque of prototype. The proposed method is able to predict the cogging torque waveform with high degree of accuracy. The amplitude is also slight higher that FEM model.

B. Angular Misalignment Permeance

As for the angular misalignment, $f_{se} = 33\%$ (1-mm deviation) is chosen to verify the effectiveness of the proposed method under angular misalignment condition. The reference point ($\gamma 0$) is set as 0°.

Before the performance analysis, the influence of section number of PMs on the MFD should be investigated to ensure the accuracy. The PMs with MD 90° are selected as the research object since the influence is much higher than other PMs.

Fig. 15(a) shows the radial components with different section numbers. It can be seen that if the tolerance is not very strict, the results could be acceptable when the section number is 1 (total 16 sections along circumferential direction and about two times of slot number). Fig. 15(b) presents the harmonics with different section numbers, it is clear that the accuracy will hardly vary when the section number is 2 (total 32 sections along circumferential direction and about three times of slot number). With section number analysis, it can be found that the section number is also related to the cyclic symmetry number; either the reference center is stator or rotor, which also confirms in [17].

It should be noted that when there is angular misalignment, the cogging torque calculation needs more accurate MFD. Therefore, the section number is still selected as 2 in this paper (about three times the slot number). After using superposition principle, the total MFD is shown in Fig. 16. It can be seen that the results match well with FE results. Again, the correction factor is still needed to improve the accuracy under angular misalignment; similar conclusion can be drawn for axis misalignment.

As previous study shown in [9], it can be found that the back EMFs have a slight change compared with normal condition. This is because the flux density increases in one position, but decreases in the opposite position, moreover, the coils of

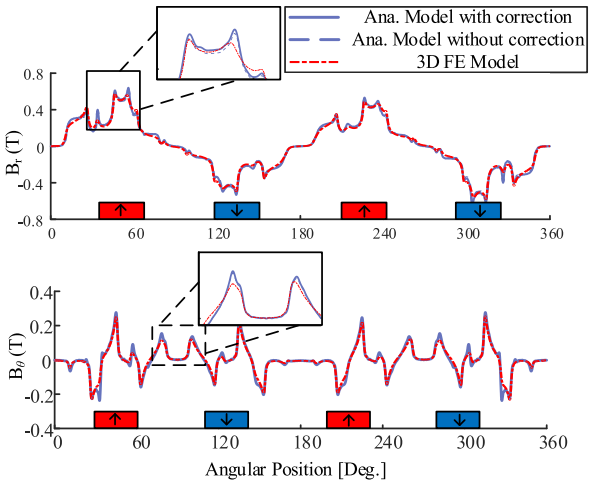

Fig. 16. Total MFD waveforms under angular misalignment.

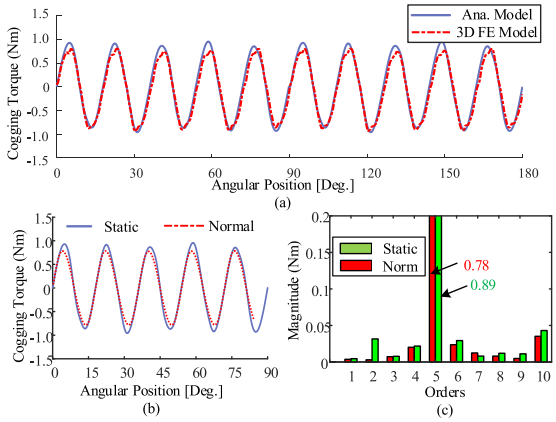

Fig. 17. Cogging torque under static angular misalignment condition. (a) Waveforms. (b) Comparison. (c) Harmonics.

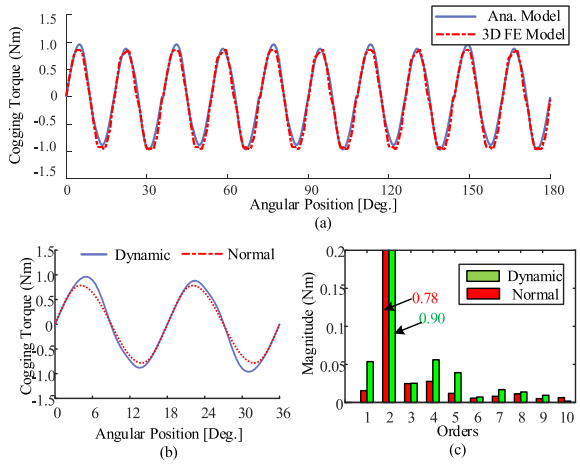

Fig. 18. Cogging torque under dynamic angular misalignment condition. (a) Waveforms. (b) Comparison. (c) Harmonics.

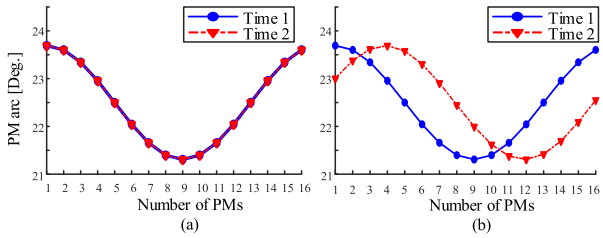

Fig. 19. PM arc under axis misalignment. (a) Static. (b) Dynamic.

investigated machine in this paper are symmetrical along circumferential direction, as a result, the changes in the back EMF of the coils of one phase cancel each other, so that the back EMF results do not change much when comparing with normal condition. Therefore, the back EMFs are not investigated in this paper.

It should be noted that when the AFPM are transformed to the approximated approach presented in this paper, the theory for RFPM could be used as reference; this is an advantage for this method. According to [20], the cogging torque periods for static and dynamic misalignment are $2p$ and N_s, respectively. In order to show clearly, only one period is given.

The Figs. 17(a) and 18(a) show the comparison of cogging torque waveforms under static and dynamic angular misalignment calculated by the proposed method and 3-D FEM model, respectively. The results show that the proposed method can predict the influence of angular misalignment; it can be clearly observed that the period and the results are acceptable. Figs. 17(b) and 18(b) compare one period waveform with the normal condition obtained by proposed method, and the corresponding fast Fourier transform (FFT) series results are shown in Figs. 17(c) and 18(c), respectively. It can be found that the amplitude is slightly increased. As is known, the angular misalignment will hardly affect the cogging torque if the cyclic symmetry is large. Therefore, for AFPM machine with 10-slot/4-pole in this paper, it is tolerance to the effect caused by angular misalignment since the cyclic symmetry number is 2. The generation mechanism of additional harmonic components due to angular misalignment for RFPM machine has been fully discussed in [21], which has referenced value for AFPM machines.

C. Axis Misalignment Permeance

As for the axis misalignment, $e_{ccs} = 4$ mm extension is chosen to verify the effectiveness of the proposed method under axis misalignment condition. It is clear that the axis misalignment can be detected easily by mechanical approach when e_{ccs} is 4 mm, however, in order to show clearly the difference with the normal condition, 4 mm is selected.

The initial angle (θ) shown in Fig. 5 is set to 0° to verify the effectiveness of the proposed method. Afterward, each PM angle can be calculated and the results are shown in Fig. 18. It can be seen that, in Fig. 19(a), the PM angle is changed sinusoidal under static axis misalignment, but it is constant under dynamic axis misalignment as shown in Fig. 19(b).

To be clear about the influence of axis misalignment on the MFD, the PMs with MD 90° are selected to investigate the aforementioned reason. Fig. 20 shows the variation of the radial components. By comparing with the normal condition, it can be

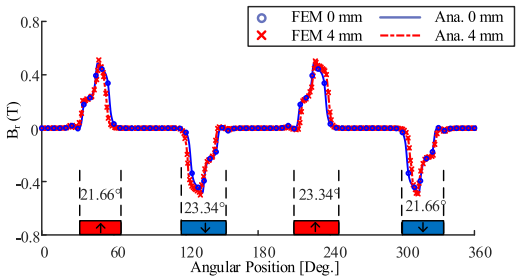

Fig. 20. Total MFD waveforms under axis misalignment.

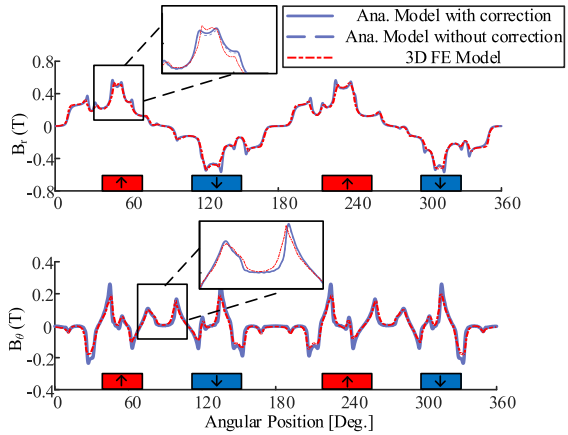

Fig. 21. Total MFD waveforms under angular misalignment.

seen that the result under axis misalignment has been shifted. This is caused by the changes of PM length under calculating reference, which can be seen in Fig. 20, and this means that the period of the flux density wave would no longer be constant.

It can be seen that the PM length varies along the circumferential direction under axis misalignment. If traditional approach is adopted to model the magnetization vector, Fourier series expansion is necessary at every step. On the other hand, the current sheet can avoid this step because it can model the PM individually, which is more straightforward to complete the calculation.

After calculating each PM and using superposition principle, the total MFD can be obtained, as shown in Fig. 21. It can be seen that the results match well with FE results.

With regard to the back EMFs under axis misalignment, it can be found that the change in length of PM is characterized by sinusoid, which means that the total length of PM is unchanged with normal condition at any time step; it can be seen in Fig. 19 that the total angle is still 90° (4 time of 22.5°). Hence, the total flux of one phase is unchanged in theory. On the other hand, the study in [8] has investigated the back EMFs under such condition. Therefore, the cogging torque is researched here.

Fig. 22(a) shows the comparison of cogging torque waveform under static axis misalignment calculated by the proposed method and 3-D FEM model. The results show that the results obtained by proposed method match well with 3-D FEM. What is more is that it can be seen that the cogging torque periods is 4 and it still obeys the theory in [20]. Fig. 22(b) and (c) shows

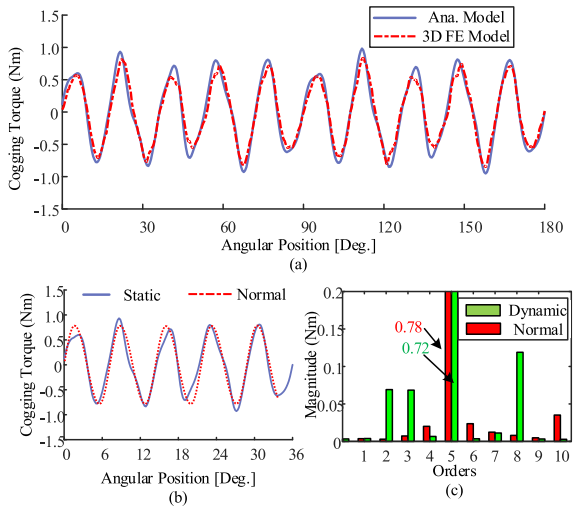

Fig. 22. Cogging torque under static axis misalignment condition. (a) Waveforms. (b) Comparison. (c) Harmonics.

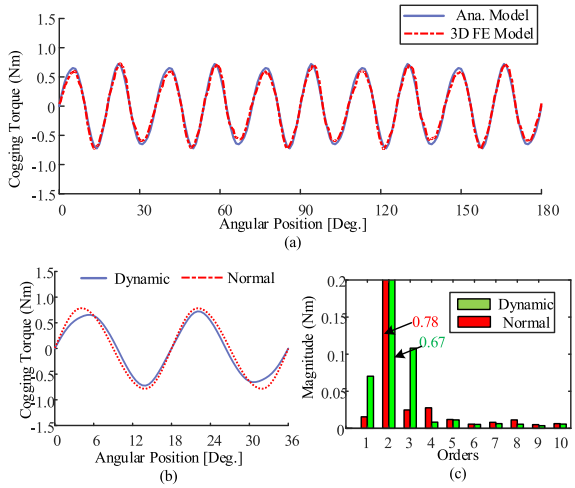

Fig. 23. Cogging torque under dynamic axis misalignment condition. (a) Waveforms. (b) Comparison. (c) Harmonics.

the results of FFT with the normal condition obtained by proposed method. It can be found that the amplitude of fundamental harmonic is slightly decreased and the static axis misalignment causes more harmonics.

Fig. 23(a) shows the comparison of cogging torque waveform under dynamic axis misalignment. It shows that the proposed model can predict the cogging torque well and the period is 10. Fig. 23(b) shows the comparison between the normal condition in one period and the corresponding FFT is shown in Fig. 23(c). Both results show that the axis misalignment hardly affects the cogging torque, and this phenomenon can also be explained by the cyclic symmetry number. In Fig. 23(c), the result shows that the critical order (fifth order) of the cogging torque is decreased significantly to 0.67 N·m, while with the first and second order sidebands of the main harmonic increased clearly due to the misalignment. This similar phenomenon is also confirmed in [18].

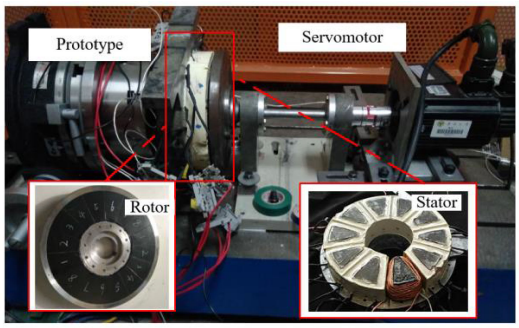

Fig. 24. Back EMFs experimental set up.

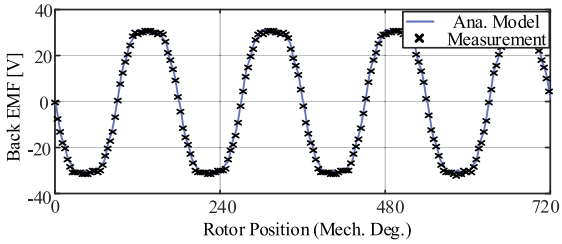

Fig. 25. EMF results.

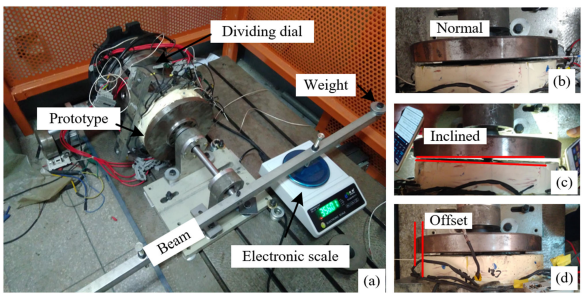

Fig. 26. Cogging torque experiment. (a) Set up. (b) Normal condition. (c) Angular misalignment. (d) Axis misalignment.

IV. Experimental Validation

The experimental setup and devices are shown in Fig. 24. In the test bench, the prototype is coupled with a servomotor via coupling. A no-load test was done at 2000 r/min. The comparison between the analytical results and the experimental results is shown in Fig. 25. It can be seen that the results match well.

AFPM machine in this paper presents a separable component that is simple in structure and convenient for testing and measuring. The test rig for cogging torque is shown in Fig. 26(a). The prototype is clamped by a dividing dial and a beam is fixed to the rotor shaft. A weight is fixed on one side of beam in order to keep the force acts on the scale at any rotor position; moreover, the weight can reduce the influence of friction. Fig. 26(b) shows the normal condition. As for the angular misalignment test, the rotor system is inclined as shown in Fig. 26(c). The axis misalignment test can be set by the similar process as shown in Fig. 26(d).

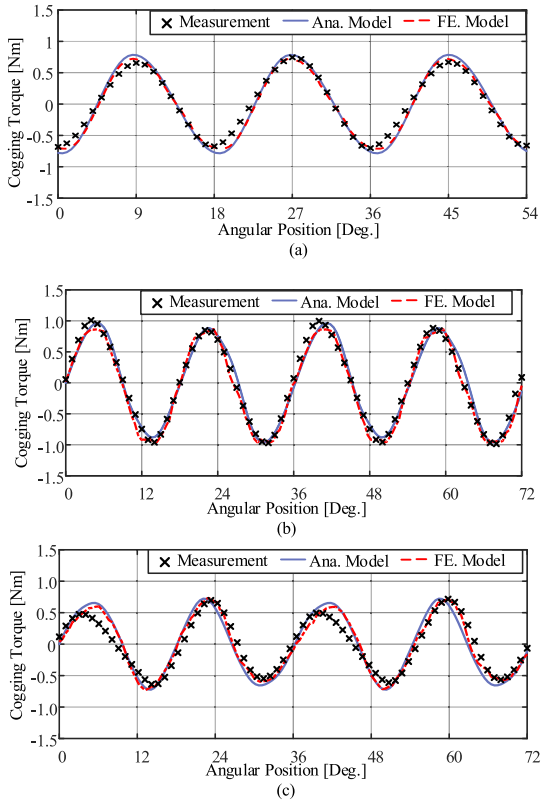

Fig. 27. Comparison between measurement, proposed, and FE model. (a) Normal condition. (b) Dynamic angular misalignment. (c) Dynamic axis misalignment.

The cogging torque waveform can be obtained by the lever principle. Fig. 27(a) shows the comparison between the proposed approaches; FE model predicted and measured cogging torque waveforms under normal condition. It can be found that an acceptable agreement has been achieved. It should be noticed that when rotating the stator to obtain the cogging torque under misalignment, they both present dynamic misalignment, which can be confirmed by the results data shown in Fig. 27(b) and (c).

V. Conclusion

In this paper, a new thought for AFPM with misalignments was presented, and consequently, an AM based on polar coordinate was developed. The calculation coordinate of AFPM was changed to the polar coordinate; thereby, the eccentricity theory for RFPM machine could be applied to AFPM machine. Four types of misalignment were researched in this paper, and the analytical results of MFD, back EMF, and the torque matched well with those of FEM and experimental results, which confirmed the validity of the proposed model. Meanwhile, the method proposed in this paper required only a few minutes to get the final results, and the computation time can be reduced remarkably maintaining the high accuracy as that of FE model, which is good for carrying out the further fault diagnosis work.

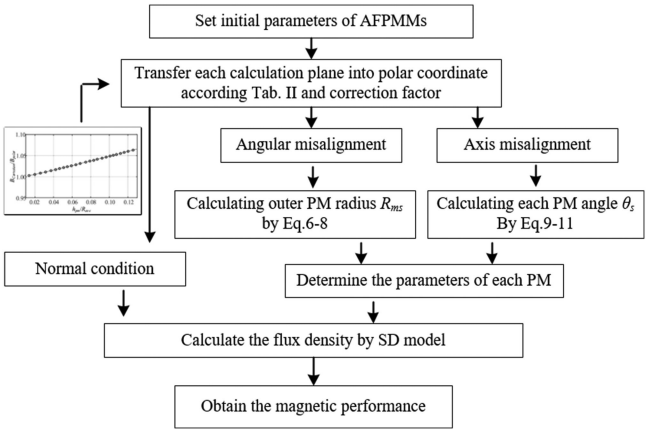

Fig. 28. Calculation flowchart.

Appendix

The calculation processes can be shown in Fig. 28.

References

[1] G. Oosthuizen, "Design of an ironless double-rotor radial flux air-cored permanent magnet machine," in *Proc. IEEE Int. Electric Mach. Drives Conf.*, 2015, pp. 683–688.

[2] O. Maloberti *et al.*, "3-D–2-D dynamic magnetic modeling of an axial flux permanent magnet motor with soft magnetic composites for hybrid electric vehicles," *IEEE Trans. Magn.*, vol. 50, no. 6, Jun. 2014, Art. no. 8201511.

[3] A. Hemeida, M. Taha, A. A. E. Abdallh, H. Vansompel, L. Dupré, and P. Sergeant, "Applicability of fractional slot axial flux permanent magnet synchronous machines in the field weakening region," *IEEE Trans. Energy Convers.*, vol. 32, no. 1, pp. 111–121, Mar. 2017.

[4] T. Mark, "Analysis of cogging torque due to manufacturing variations in fractional pitch permanent magnet synchronous machines," *Ph.D. Thesis*, School Eng. Inf. Technol., Charles Darwin Univ., Australia, 2013.

[5] A. Di Gerlando, G. M. Foglia, M. F. Iacchetti, and R. Perini, "Effects of manufacturing imperfections in concentrated coil axial flux PM machines: Evaluation and tests," *IEEE Trans. Ind. Electron.*, vol. 61, no. 9, pp. 5012–5024, Sep. 2014.

[6] A. Di Gerlando, G. M. Foglia, M. F. Iacchetti, and R. Perini, "Evaluation of manufacturing dissymmetry effects in axial flux permanent-magnet machines: Analysis method based on field functions," *IEEE Trans. Magn.*, vol. 48, no. 6, pp. 1995–2008, Jun. 2012.

[7] E. Ajily, M. Ardebili, and K. Abbaszadeh, "Magnet defect and rotor eccentricity modeling in axial-flux permanent-magnet machines via 3-D field reconstruction method," *IEEE Trans. Energy Convers.*, vol. 31, no. 2, pp. 486–495, Jun. 2016.

[8] Z. Q. Zhu, L. J. Wu, and Z. P. Xia, "An accurate subdomain model for magnetic field computation in slotted surface-mounted permanent-magnet machines," *IEEE Trans. Magn.*, vol. 46, no. 4, pp. 1100–1115, Apr. 2010.

[9] B. Guo, Y. Huang, F. Peng, Y. Guo, and J. Zhu, "Analytical modeling of manufacturing imperfections in double-rotor axial flux PM machines: Effects on back EMF," *IEEE Trans. Magn.*, vol. 53, no. 6, pp. 1–5, Jun. 2017.

[10] N. Ertugrul, R. Hasegawa, W. L. Soong, J. Gayler, S. Kloeden, and S. Kahourzade, "A novel tapered rotating electrical machine topology utilizing cut amorphous magnetic material," *IEEE Trans. Magn.*, vol. 51, no. 7, pp. 1–6, Jul. 2015.

[11] H. Hu, J. Zhao, X. Liu, and Y. Guo, "Magnetic field and force calculation in linear permanent-magnet synchronous machines accounting for longitudinal end effect," *IEEE Trans. Ind. Electron.*, vol. 63, no. 12, pp. 7632–7643, Dec. 2016.

[12] A. Hemeida and P. Sergeant, "Analytical modeling of surface PMSM using a combined solution of Maxwell's equations and magnetic equivalent circuit," *IEEE Trans. Magn.*, vol. 50, no. 12, pp. 1–13, Dec. 2014.

[13] Z. Q. Zhu, D. Howe, and C. C. Chan, "Improved analytical model for predicting the magnetic field distribution in brushless permanent-magnet machines," *IEEE Trans. Magn.*, vol. 38, no. 1, pp. 229–238, Jan. 2002.

[14] B. Guo, Y. Huang, F. Peng, and J. N. Dong, "General analytical modelling for magnet demagnetization in surface mounted permanent magnet machines," *IEEE Trans. Ind. Electron.*, vol. 66, no. 8, pp. 5830–5838, Aug. 2019.

[15] Y. Zhou, H. Li, G. Meng, S. Zhou, and Q. Cao, "Analytical calculation of magnetic field and cogging torque in surface-mounted permanent magnet machines accounting for any eccentric rotor shape," *IEEE Trans. Ind. Electron.*, vol. 62, no. 6, pp. 3438–3447, Jun. 2015.

[16] S. M. Mirimani, A. Vahedi, F. Marignetti, and R. Di Stefano, "An online method for static eccentricity fault detection in axial flux machines," *IEEE Trans. Ind. Electron.*, vol. 62, no. 3, pp. 1931–1942, Mar. 2015.

[17] Y. Li, Q. Lu, Z. Q. Zhu, D. Wu, and G. Li, "Superposition method for cogging torque prediction in permanent magnet machines with rotor eccentricity," *IEEE Trans. Magn.*, vol. 52, no. 6, pp. 1–10, Jun. 2016.

[18] M. Thiele and G. Heins, "Computationally efficient method for identifying manufacturing induced rotor and stator misalignment in permanent magnet brushless machines," *IEEE Trans. Ind. Appl.*, vol. 52, no. 4, pp. 3033–3040, Jul./Aug. 2016.

[19] G. Houdouin, G. Barakat, B. Dakyo, and E. Destobbeleer, "A winding function theory based global method for the simulation of faulty induction machines," in *Proc. IEEE Int. Electric Mach. Drives Conf.*, vol. 1, 2003, pp. 297–303.

[20] L. Gasparin, A. Cernigoj, S. Markic, and R. Fiser, "Additional cogging torque components in permanent-magnet motors due to manufacturing imperfections," *IEEE Trans. Magn.*, vol. 45, no. 3, pp. 1210–1213, Mar. 2009.

[21] Z. Q. Zhu, L. J. Wu, and M. L. M. Jamil, "Influence of pole and slot number combinations on cogging torque in permanent magnet machines with static and rotating eccentricities," in *Proc. IEEE Energy Convers. Congr. Expo.*, 2013, pp. 2834–2841.

Baocheng Guo (S'14–M'18) received the B.E. degree from the China University of Petroleum, Qingdao, China, in 2009, the M.E. degree from the Harbin University of Science and Technology, Harbin, China, in 2014, and the Ph.D. degree from Southeast University, Nanjing, China, in 2017, all in electrical engineering.

Since 2018, he has been a Postdoc Researcher with Southeast University, in 2018. His research interests include the electromagnetic field computation and development of fast multi-physics models of electrical machines.

Yunkai Huang received the M.Sc. and Ph.D. degrees in electrical engineering from Southeast University, Nanjing, China, in 2001 and 2007, respectively.

In 2015, he joined the electrical engineering with the School of Electrical Engineering, Southeast University, where he is currently a Professor in Electrical Engineering. His research interests include design and control of permanent magnet machine and high speed machine, applications in domestic appliances, electric vehicles, railway traction, all-electric ships, more-electric aircraft, and wind power generation systems.

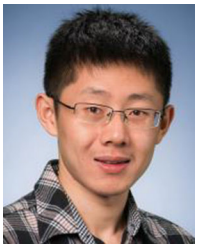

Fei Peng (S'15–M'16) received the B.S. and M.S. degrees in electrical engineering from Southeast University, Nanjing, China, in 2010 and 2012, respectively. He received the Ph.D. degree in electrical and computer engineering from McMaster University, Hamilton, ON, Canada, in 2016.

After that, in 2016, he joined the McMaster Institute for Automotive Research and Technology (MacAUTO), McMaster University in 2016. In 2016, he joined the School of Electrical Engineering at Southeast University, Nanjing, China, as an Assistant Professor. His research interests include optimal design and control of power converters, modeling, and digital control of motor drives.

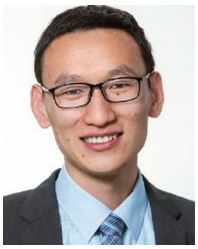

Jianning Dong (S'10–M'17) received the B.S. and Ph.D. degrees in electrical engineering from Southeast University, Nanjing, China, in 2010 and 2015, respectively.

In 2015, he joined McMaster Automotive Resource Centre (MARC), McMaster University, Hamilton, ON, Canada, as a Postdoc Researcher in 2015. He has been an Assistant Professor in Electrical Engineering with the Delft University of Technology, Delft, The Netherlands, since 2016. His research interests include design, modeling, and control of electromechanical systems.

Yongjian Li (M'10) was born in Hebei, China, in 1978. He received the B.E., M.E., and Ph.D. degrees from the Hebei University of Technology (HEBUT), Tianjin, China, in 2002, 2007, and 2011, respectively.

From 2009 to 2011, he was an Assistant Professor in Electromagnetic with the University of Technology Sydney, Ultimo, NSW, Australia. As a Visiting Scholar, he visited Ottawa University, Ottawa, ON, Canada, from 2016 to 2017. In 2002, he joined HEBUT, where he is currently a Professor in Electromagnetic with the School of Electrical Engineering in 2002, and also the Deputy Director of the State Key Laboratory of Reliability and Intelligence of Electrical Equipment. His research interests include measurement magnetic properties, modeling of magnetic materials, and power electronics.